

Survey strategies for the first supernovae with JWST

Tilman Hartwig^{1,2*}, Volker Bromm³ and Abraham Loeb⁴

¹*Sorbonne Universités, UPMC Univ Paris 06, UMR 7095, Institut d’Astrophysique de Paris, F-75014 Paris, France*

²*CNRS, UMR 7095, Institut d’Astrophysique de Paris, F-75014, Paris, France*

³*Department of Astronomy, University of Texas, Austin, Texas 78712, USA*

⁴*Department of Astronomy, Harvard University, 60 Garden Street, Cambridge, MA 02138, USA*

14 December 2024

ABSTRACT

Pair-instability supernovae (PISNe) are very luminous explosions of massive, low metallicity stars. They can potentially be observed out to high redshifts due to their high explosion energies, thus providing a probe of the Universe prior to reionisation. The near-infrared camera, NIRCam, on board the *James Webb Space Telescope* is ideally suited for detecting their redshifted ultraviolet emission. We calculate the photometric signature of high-redshift PISNe and derive the optimal survey strategy for identifying their prompt emission and possible afterglow. We differentiate between PISNe and other sources that could have a similar photometric signature, such as active galactic nuclei or high redshift galaxies. We demonstrate that the optimal survey strategy, which maximises the visibility time of the PISN lightcurve per invested exposure time, consists of the two wide-band filters F200W and F356W with an exposure time of 600 s. The PISN afterglow, caused by nebular emission and reverberation, is very faint and requires unfeasibly long exposure times to be uniquely identified. However, this afterglow would be visible for several hundred years, about two orders of magnitude longer than the prompt emission, rendering PISNe promising targets for future, even more powerful telescopes.

Key words: early Universe – cosmology: dark ages, reionization, first stars – stars: Pop III – supernovae: general

1 INTRODUCTION

The frontiers of astronomy are approaching the epoch when the first generation of stars and galaxies were born. These first, so-called Population III (Pop III), stars are the key for understanding the formation of all subsequent structures in the Universe: they lit up the Universe when its age was less than 5% of its current age, they might have provided the seeds for supermassive black holes, and their creation of heavy elements had set the scene for the emergence of the first galaxies. Pop III stars are believed to have formed at redshifts $z = 10 - 25$ and to have had a higher characteristic mass than present-day stars, due to the lack of metals as efficient coolants at high redshift (Bromm et al. 1999; Abel et al. 2002; Yoshida et al. 2003). Their exact mass range and distribution is needed for accurately determining the ensuing radiative and chemical feedback, but it is still debated (Stacy et al. 2010; Clark et al. 2011; Hosokawa et al. 2011; Susa et al. 2014; Hirano et al. 2014; Hartwig et al. 2015; Stacy et al. 2016; de Bressan et al. 2017; Hirano

& Bromm 2017). In addition to existing numerical simulations, it is important to obtain observational evidence to better constrain the initial mass function (IMF) of the first stars.

Low-metallicity stars in the mass range $140 - 260 M_{\odot}$ are expected to go through a pair-instability supernova (PISN) at the end of their stellar lifetime. These very luminous explosions with energies of 10^{51-53} erg are triggered by electron-positron pair production in the hot core of massive stars. The resulting reduction in radiation support causes the core to collapse, thus igniting explosive oxygen and silicon burning which completely disrupts the star, leaving no compact remnant behind (Rakavy & Shaviv 1967; Barkat et al. 1967; Fraley 1968; Bond et al. 1984; Fryer et al. 2001). PISNe are powered by the diffusion of the shock energy, the interaction of the ejecta with the surrounding medium, and by a major contribution from radioactive decay of nickel over a time of about one year (Kasen et al. 2011). At slightly lower masses, metal-free stars can also encounter pulsational PISNe, where the pair production does not completely disrupt the star, but initiates a pulsational sequence of several core contractions, which are individually not power-

* E-mail: tilman.hartwig@ipmu.jp

ful enough to unbind the star (Whalen et al. 2013; Spera & Mapelli 2017; Woosley 2017; Tolstov et al. 2017). With stellar rotation, PISNe can occur down to stellar masses of $\sim 80 M_{\odot}$, avoiding the pulsational phase (Chatzopoulos & Wheeler 2012; Yoon et al. 2012; Smidt et al. 2015). Other types of superluminous supernovae (SLSNe) were proposed in the literature as well (Umeda & Nomoto 2003; Tominaga 2009; Moriya et al. 2010; Gal-Yam 2012; Nicholl et al. 2013; Yoshida et al. 2014; Abbott et al. 2017). Cooke et al. (2012) reported the detection of two SLSNe at $z = 2$ and $z = 4$ with slowly evolving lightcurves. They predicted that the rate of SLSNe at higher redshift is one order of magnitude higher than in the local Universe.

The possibility of detecting PISNe at high redshift and thereby constraining the properties of their stellar progenitors has been previously discussed (Mackey et al. 2003; Scannapieco et al. 2005; Whalen et al. 2013; Pan & Loeb 2013; de Souza et al. 2014; Wang et al. 2017). Those predictions are based on theoretical models of PISN lightcurves with multidimensional radiative transfer codes (Scannapieco et al. 2005; Woosley et al. 2007; Kasen et al. 2011; Pan et al. 2012; Chen et al. 2014; Jerkstrand et al. 2016; Kozyreva et al. 2017; Gilmer et al. 2017). Cosmological simulations and semi-analytical models of structure formation predict the PISN rate as a function of redshift (Miralda-Escudé & Rees 1997; Wise & Abel 2005; Hummel et al. 2012; Pan et al. 2012; Johnson et al. 2013; Tanaka et al. 2013; Magg et al. 2016), concluding that PISNe are rare events that require an optimised survey strategy and a large field of view to detect them. However, a direct detection would be extremely valuable for our understanding of Pop III star formation, because this mass range has not been probed by stellar archaeology (but see Aoki et al. 2014).

The main focus of this paper is to find efficient survey strategies to detect PISNe at high redshift with the *James Webb Space Telescope (JWST)*¹, as well as other next-generation facilities. Based on realistic lightcurves, we determine their photometric signature and derive the optimal survey strategy by maximising the visibility time of a PISN event for a given exposure time. We present the optimal 2-filter combination and exposure time for the prompt emission. We also discuss the possibility to detect the PISN afterglow, caused by nebular emission and reverberation in the surrounding gas. We thus introduce a novel probe of the pre-galactic medium, whose utility, however, has to await the advent of even more powerful telescopes in the future.

2 METHODOLOGY

The first stars are expected to form as small multiples in metal-free gas, with a distribution that extends to high masses (Stacy et al. 2010; Clark et al. 2011; Greif et al. 2011). As a result, they produce a strong UV flux, which partially or completely ionises the surrounding interstellar medium (ISM). If at least one star is in the mass range $140 - 260 M_{\odot}$, a PISN will be triggered. In this section, we describe how we model the ISM, the underlying stellar population, the radiative feedback on the ISM, and the inter-

action of the PISN with the gas. We also consider other astrophysical sources that exhibit a similar spectral energy distribution (SED), thus possibly mimicking a PISN signature.

2.1 Single Stellar Population

We assume that the PISN progenitor stars are embedded in a metal-free stellar cluster or group. Consequently, we also account for the radiative feedback from the underlying stellar population, resulting in the build-up of an HII region. To generate synthetic spectra of these primordial clusters, we consider single stellar population (SSP) models by Schaerer (2002), where Pop III stars radiate close to a blackbody (Bromm et al. 2001). We have verified that our modeling agrees with the Pop III SEDs by Zackrisson et al. (2011).

As a fiducial model, we use a logarithmically-flat IMF in the range $M_{\min} = 3 M_{\odot}$ to $M_{\max} = 300 M_{\odot}$, motivated by simulations (Clark et al. 2011; Greif et al. 2011; Dopcke et al. 2013) and empirical hints (Aoki et al. 2014). Given that metal-free stars with masses of $140 - 260 M_{\odot}$ are predicted to explode as PISNe (Heger & Woosley 2002), we expect on average one PISN event per $500 M_{\odot}$ in Pop III stars. We further assume that all Pop III stars form in one initial burst with a duration of $\Delta t_{\text{sb}} = 10^5$ yr, which corresponds to the free-fall time at typical densities in the pre-stellar core (Stacy et al. 2010; Clark et al. 2011). This is short compared to typical stellar lifetimes of over several million years.

The rest-frame time interval over which the prompt PISN emission is bright extends for ~ 1 yr, whereas the time over which stars explode as PISN, averaged over their different progenitor masses, is $\Delta t_{\text{PISN}} \approx 10^5$ yr. Together with Δt_{sb} , this yields an interval of $\sim 2 \times 10^5$ yr over which PISNe are possible for a given primordial galaxy. Consequently, one has to be lucky to observe such a galaxy at the right moment to detect a PISN signature. Even for a galaxy with a total mass of $10^5 M_{\odot}$ in Pop III stars, and hence ~ 200 expected PISN explosions, the probability to observe two PISNe at the same time is negligibly small. We hence focus on the case in which one single PISN explodes at a time.

2.2 PISN spectra

We use the tabulated PISN spectra by Kasen et al. (2011), in the form of the SED of PISNe for different times after the explosion. Specifically, we employ the model of red supergiants, since Pop III stars in the PISN mass range are expected to have convective envelopes, which can mix the central metals with the outer hydrogen layers. The prompt emission of each PISN is brighter than the underlying stellar population for only about 1 yr in the source frame, and previous studies have focused on the detection of this prompt emission (Weinmann & Lilly 2005; Frost et al. 2009; Hummel et al. 2012; Whalen et al. 2013; de Souza et al. 2013, 2014). Even if this time interval gets extended due to cosmological expansion by a factor of ~ 10 , it is still very unlikely to detect this prompt emission in high redshift surveys and we have to determine the optimal diagnostic. We consider two additional effects in our modeling, which stretch the time of possible observation to several hundreds of years in the source rest-frame: nebular emission from the ionised gas and the geometrical echo effect of the ambient medium.

¹ <https://www.jwst.nasa.gov>

2.3 Nebular Emission

To model the observed SED of the superposed Pop III stellar population and a possible PISN contribution, we use the photoionisation code CLOUDY (Ferland et al. 2013), with gas of primordial composition and no dust. For the geometry and density of the ambient gas we assume three different models: a constant gas density of $n_{\text{H}} = 1 \text{ cm}^{-3}$ or $n_{\text{H}} = 100 \text{ cm}^{-3}$ out to a radius of 100 pc, falling off as r^{-2} beyond (Wang et al. 2012), or the idealized case of very low ambient gas density, for simplicity represented as $n_{\text{H}} = 0$. The first two models correspond to the typical conditions in a minihalo ($M_{\text{vir}} = 10^6 M_{\odot}$) and an atomic cooling halo ($T_{\text{vir}} \gtrsim 10^4 \text{ K}$), respectively. The last model, lacking any re-processing of the emitted radiation, corresponds to a negligibly low nebular density, caused by strong stellar feedback, or the clumpiness of the gas into a few high-density regions with a small covering fraction (Santos et al. 2002). The assumed density is in agreement with observations of the circumburst medium of the gamma-ray burst GRB090423 at $z = 8.2$ (Chandra et al. 2010). For the inner radius of the spherical gas distribution we assume 1 pc, which corresponds to the size of the Pop III star-forming region. We have verified that the exact choice of this value has no significant influence on the final results.

The Strömgen radius, within which gas is completely ionised, is given by

$$R_{\text{S}} = \left(\frac{3Q_{\text{H}}}{4\pi\alpha n_{\text{H}}^2} \right)^{1/3} \approx 66 \text{ pc} \left(\frac{M_{*}}{10^5 M_{\odot}} \right)^{1/3} \left(\frac{n_{\text{H}}}{100 \text{ cm}^{-3}} \right)^{-2/3} \quad (1)$$

with an ionising photon flux of Q_{H} , a recombination coefficient of $\alpha = 5 \times 10^{-13} \text{ cm}^3 \text{ s}^{-1}$, and a total mass in Pop III stars of M_{*} . To relate the flux of ionising photons to the stellar mass, we use tabulated stellar evolution models (Schaerer 2002), averaged over the IMF, whereas the exact upper limit of the IMF for this average has only a minor influence (Bromm et al. 2001). We note that the Strömgen radius is smaller than the constant density core for a gas density of $n_{\text{H}} = 100 \text{ cm}^{-3}$, but larger for a gas density of $n_{\text{H}} = 1 \text{ cm}^{-3}$. This indicates that the gas is already completely ionised when a PISN explodes in a minihalo, and we do not expect a significant additional contribution from nebular emission in this case (Zackrisson et al. 2011).

The contribution from the PISN to the nebular emission depends on the ionising efficiency of the underlying Pop III stellar population: there is a critical stellar mass for a given ISM density, above which the Pop III stars alone already completely ionise the ISM, thus dominating the nebular emission. In this scenario, the ionising radiation from the PISN does not additionally contribute to the recombination line flux. For a gas density of $n_{\text{H}} = 1 \text{ cm}^{-3}$, the critical stellar mass for which Pop III stars ionise half the ISM volume and dominate the nebular emission is $M_{*} < 100 M_{\odot}$. For minihalos with typical densities of $\sim 1 \text{ cm}^{-3}$ we do therefore not expect a nebular signature from PISNe, but only their prompt emission. The SED of a single stellar population (SSP) with and without the contribution of different PISNe can be seen in Fig. 1. The prompt PISN emission is about two orders of magnitude brighter than the underlying Pop III stellar population.

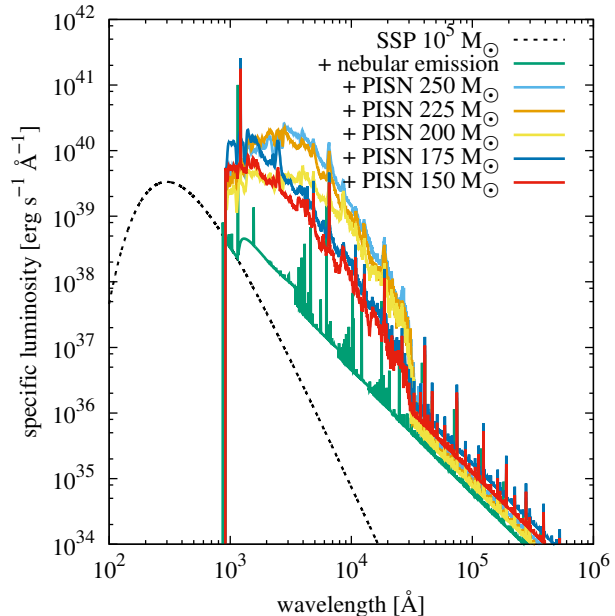


Figure 1. SEDs of a SSP of $10^5 M_{\odot}$, with and without PISN contribution, and an ambient gas density of $n_{\text{H}} = 100 \text{ cm}^{-3}$. The PISN SEDs are averaged over the time of explosion, weighted by their bolometric luminosity. Photons bluewards of 912 \AA are absorbed by the neutral surrounding medium, and re-emitted in the IR.

2.3.1 Recombination

The nebular emission caused by the PISN decays over the recombination time scale

$$t_{\text{rec}} = \frac{1}{n_e \alpha} \simeq 400 \text{ yr} \left(\frac{n_e}{10^2 \text{ cm}^{-3}} \right)^{-1}, \quad (2)$$

where $n_e \simeq n_{\text{H}}$. This time scale is between the characteristic time scale of the PISN light curve ($\lesssim 1 \text{ yr}$) and the typical stellar lifetimes of several Myr. We can consequently assume that the energy input from the PISN is almost instantaneous and that the SED of the underlying stellar population does not significantly change over t_{rec} . We model the nebular emission self-consistently with CLOUDY, assuming a time-dependent incident radiation field. The resulting time evolution of the SED can be seen in Fig. 2. Already 3 yr after the explosion, the prompt emission decayed and only a few recombination lines render the PISN afterglow brighter than the underlying stellar population. The additional nebular emission from the PISN derives almost exclusively from recombination lines, with only a small contribution of free-free emission to the continuum.

2.3.2 Geometrical echo effect

The light-crossing time for a spherical gas cloud with radius $R = 100 \text{ pc}$ is $2R/c \approx 650 \text{ yr}$, which is comparable to the recombination time. Consequently, we also have to take into account geometrical effects of the ambient gas and the reverberation that is created by photons that are absorbed and re-emitted by gas off the line of sight. We assume a central energy source that emits isotropically in all directions, embedded in a spherical ambient medium and an observer at infinity. Photons get absorbed and might be re-emitted

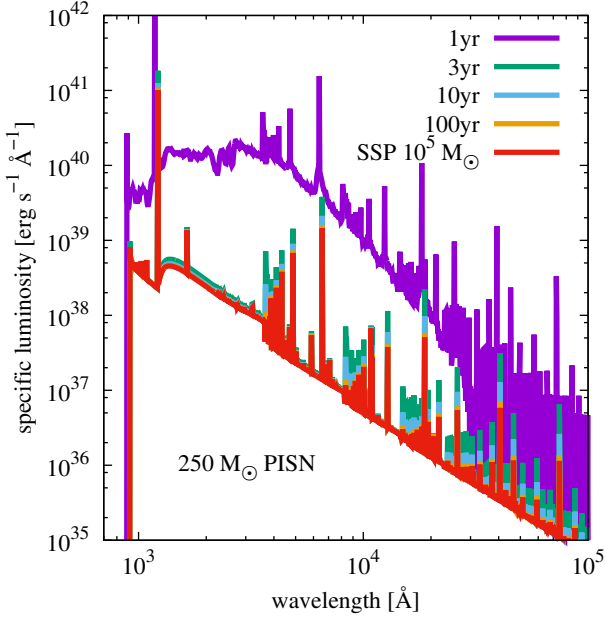


Figure 2. Spectral evolution in the PISN host. SEDs of a $10^5 M_{\odot}$ SSP (red) and the time evolution of the SED after one PISN with a progenitor mass of $250 M_{\odot}$ explodes. Initially, the PISN is about two orders of magnitude brighter than the stellar cluster, but its contribution rapidly decays, over several hundred years, back to its original value.

into the direction of the observer, but they will arrive later at the observer than photons that are directly emitted into the observer’s direction. The locus for which photons have the same travel time to the observer is a paraboloid. The cross-sectional area of this paraboloid with a sphere of gas of radius R as a function of time is given by

$$A(t) = \frac{8\pi}{3} \sqrt{ct} \left(R - \frac{ct}{2} \right)^{3/2}. \quad (3)$$

The observed SED is a convolution of SEDs emitted at different times

$$F_{\lambda}(t) = \int_0^{2R/c} dt' F_{\lambda}(t-t') N(t'), \quad (4)$$

where $N(t')$ represents the surface of the paraboloid, normalised over the convolution interval,

$$N(t') = \frac{A(t')}{\int_0^{2R/c} A(t') dt'} = \frac{4\sqrt{2}}{\pi} \frac{c}{R^3} \sqrt{ct'} \left(R - \frac{ct'}{2} \right)^{3/2}. \quad (5)$$

We add this echo effect in post-processing and do not treat it self-consistently, because a proper treatment would require full 3D radiation-hydrodynamics simulations, which is beyond the scope of this paper.

The radiative transfer of Lyman- α ($\text{Ly}\alpha$) photons should be studied in more detail, because they contribute a significant fraction of the nebular emission. $\text{Ly}\alpha$ is a resonant line and $\text{Ly}\alpha$ photons do generally not escape the ISM in the core of the line at 1216 \AA , but they get scattered into the Lorentz wings of the profile, where the effective cross section is much smaller, such that escape becomes possible. The optical depth in the line centre is (Smith et al. 2015)

$$\tau \approx 6 \times 10^6 \left(\frac{N_{\text{HI}}}{10^{20} \text{ cm}^{-2}} \right), \quad (6)$$

where N_{HI} is the column density of neutral hydrogen. This is equal to the average number of scatterings before the $\text{Ly}\alpha$ photons escape the ISM. The maximum column density of HI in our fiducial model is given by $N_{\text{HI}} \approx 2 \times 10^{22} \text{ cm}^{-2}$, assuming an ionized IGM. In this case, photons get scattered up to $\sim 3\%$ from the line centre, until the optical depth in the wings is below unity (Smith et al. 2015). The average displacement and broadening of the $\text{Ly}\alpha$ line is approximately $\Delta\lambda = 0.03\lambda_0 = 36 \text{ \AA}$, corresponding to $0.03 \mu\text{m}$ in the observer frame for a typical source at $z = 9$. Even in this very conservative scenario, the average line broadening due to resonant scattering is one order of magnitude below the typical width of the relevant *JWST* wide-band filters. Since the resonant scattering of $\text{Ly}\alpha$ photons can be assumed to be energy conserving (Draine 2011), our geometrical treatment in post-processing does not change the filter-averaged observed flux. The detailed physics of the escape of $\text{Ly}\alpha$ radiation from HI and HII regions is complex (see, e.g., Dijkstra et al. 2006; Draine 2011; Smith et al. 2015, 2017), and a redshift dependent radiative transfer calculation is necessary to fully access the broadening of all relevant lines. As we will see below, the reprocessed radiation is significantly below the detection limits of *JWST* and we do not expect a proper treatment of radiative transfer to alter this result.

2.3.3 Chemical and Mechanical feedback

Besides the radiative input, a PISN will also chemically enrich the ISM and affect the gas density by mechanical feedback. However, the time until the metal-rich shock front reaches the Strömngren radius and could affect the nebular emission is $\gtrsim 2500 \text{ yr}$ for a gas density of $n_{\text{H}} = 100 \text{ cm}^{-3}$ and a shock velocity of $\lesssim 0.1c$ (Kasen et al. 2011). Consequently, chemical and mechanical feedback do not affect the nebular emission for at least 2500 yr after the explosion of a PISN.

2.4 NIRCam filters

NIRCam, the near-infrared (NIR) photometer on *JWST* has one short-wavelength channel and one long-wavelength channel, which together cover the range of $0.5 - 5 \mu\text{m}$. This makes NIRCam the perfect instrument to probe high-redshift galaxies, whose strong rest-frame UV emission gets shifted into the NIR in the observer frame. We show the throughput² and the observer frame PISNe SEDs in Fig. 3. For the calculation of the luminosity distance, we assume a flat Universe with cosmological parameters determined by the *Planck satellite* (Planck Collaboration et al. 2016).

3 PHOTOMETRIC SIGNATURES

3.1 SEDs of high redshift sources

We first present the resulting SEDs of the PISNe, their time evolution, and the effects of nebular emission and reverberation. In addition, we construct the SEDs of other sources at high redshift, which could have the same photometric signature as PISNe and hence confuse their detection.

² <http://www.stsci.edu/jwst>

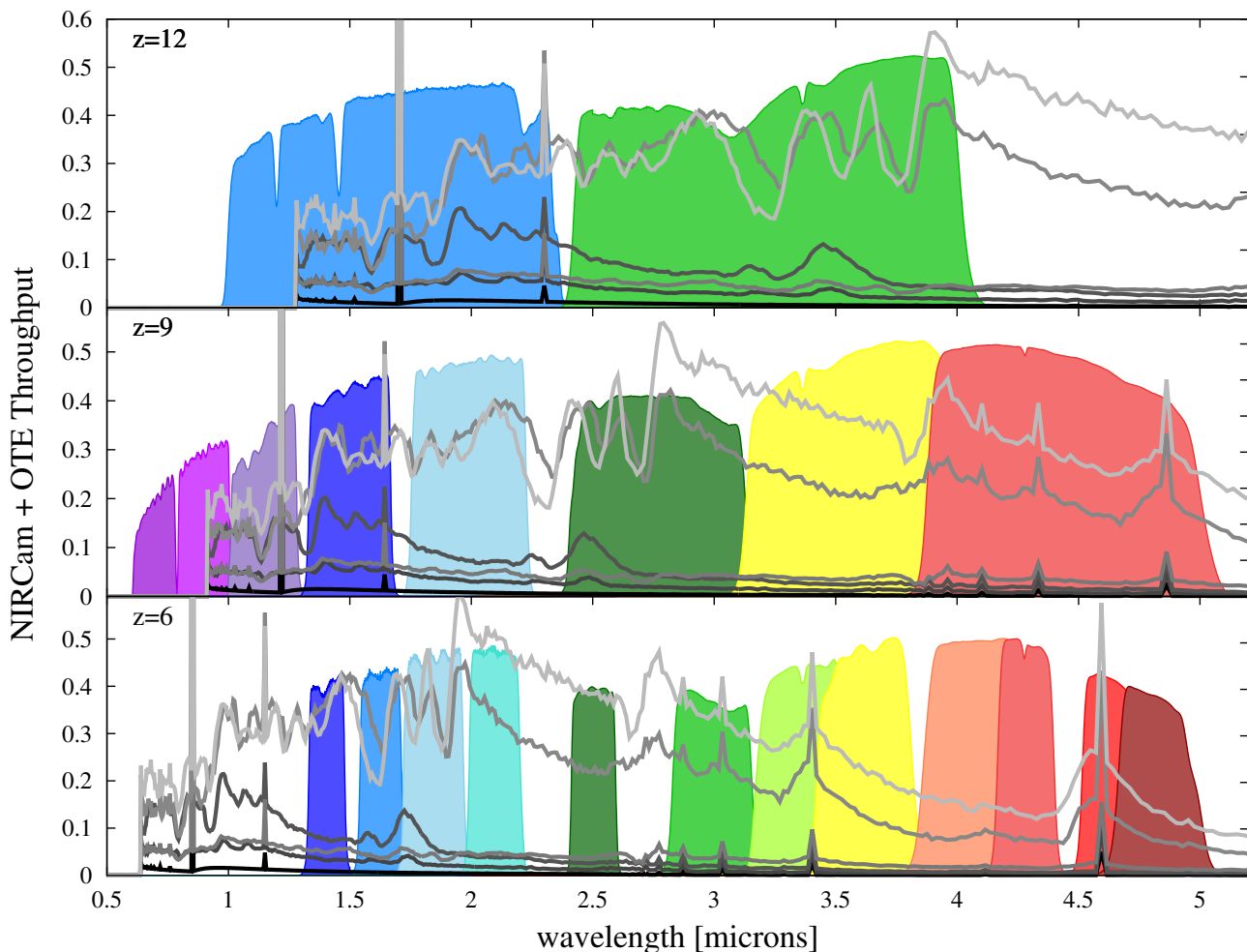


Figure 3. Filter throughputs for NIRCam and the Optical Telescope Element (OTE), superposed with the SEDs of a $10^5 M_{\odot}$ SSP (black) and of PISNe at different redshifts for different progenitor masses from $150 M_{\odot}$ (dark grey) to $250 M_{\odot}$ (light grey) with nebular emission. With increasing redshift, the flux is smaller and the SEDs shift to longer wavelengths. The selection of the appropriate filter is a trade-off between wide band filters, which have a higher sensitivity due to their higher band widths and narrow band filter, which are better suited to detect characteristic features in the SED.

3.1.1 PISNe

For the low density case, and that without any ambient medium, there is no additional afterglow or echo effect because the underlying SSP already keeps all the gas ionised (Zackrisson et al. 2011), as we show in Fig. 4. We only expect to see the prompt emission in these cases over a typical time scale of one year.

In Fig. 5, we compare the bolometric light curves after SN explosion with and without the echo effect. The reprocessing of the prompt emission stretches the lightcurve from ~ 1 yr to $\gtrsim 10$ yr and hence increases the time interval of possible detection. However, the recombination line emission decays exponentially towards the contribution from the nebular emission powered by the underlying stellar population. This yields luminosities of the reprocessed radiation that are brighter by only a factor of a few than the stellar population for $\gtrsim 1$ yr after the PISN explosion. The echo effect smooths the lightcurve over the light crossing time of the ISM. Although this increases the time interval in which we can detect PISNe by more than two orders of magnitude,

the luminosity of the PISN lightcurve is reduced by about two orders of magnitude due to conservation of the explosion energy. In Sec. 3.3, we discuss observational strategies and constraints on how to detect this faint afterglow signature and identify it as a PISN.

3.1.2 AGN

The typical PISN (averaged over progenitor masses and time after explosion) has a luminosity of $\sim 10^{43}$ erg s $^{-1}$ and peaks at ~ 200 nm. An AGN with a BH mass of $\sim 10^7 M_{\odot}$ peaks in the same wavelength range and has the same luminosity as a typical PISN for an Eddington rate of 1% (Volonteri et al. 2017). We model the emission from a typical broad line region (BLR) illuminated by such an AGN with CLOUDY, assuming a density of $n_{\text{H}} = 10^{10}$ cm $^{-3}$ and solar metallicity for the BLR. A comparison of the SEDs is shown in Fig. 6.

Direct collapse black holes (DCBHs) are an advocated sub-type of high redshift quasars that form due to the isothermal collapse of a pristine protogalaxy under the influence of a nearby photodissociating source (Bromm &

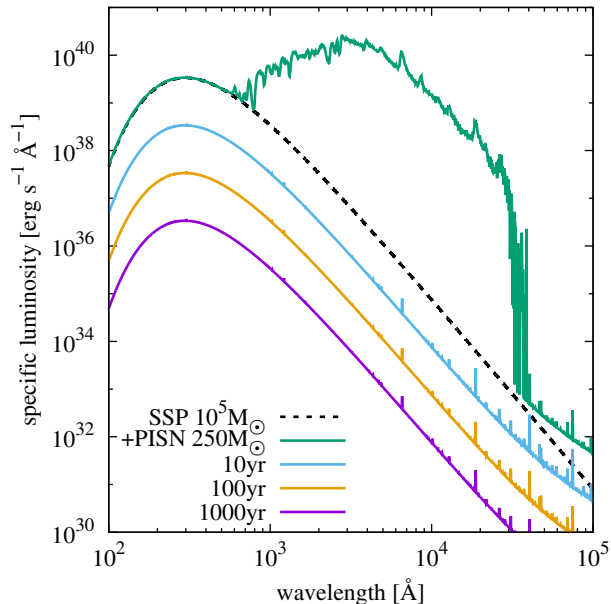


Figure 4. SEDs of the underlying SSP (black dashed) with the contribution of one PISN of $250 M_{\odot}$ (green solid) for an ambient density of $n_{\text{H}} = 1 \text{ cm}^{-3}$. The subsequent time evolution of the nebular emission is offset by 1 dex for better illustration. Due to the low gas density, all the gas in the minihalo is ionised by the SSP and the additional contribution to nebular emission from the PISN is negligible.

Loeb 2003). The isothermal collapse of pristine protogalaxies can yield seed BHs with masses of up to $\sim 10^5 M_{\odot}$, which can then further accrete gas to become more massive. These accreting DCBHs might also be detectable with *JWST* (Pacucci et al. 2016; Natarajan et al. 2017), but due to their small number density (Habouzit et al. 2016), we do not explicitly account for them, because they will not be the most abundant sources observed with *JWST*.

3.1.3 Galaxies

We also verify that our proposed photometric diagnostic is suited to distinguish a PISN from a typical high-redshift galaxy. We use the SEDs by Barrow et al. (2017), who present synthetic observations of $z \geq 6$ galaxies, based on the Renaissance simulation. They demonstrate that there is no “typical” high redshift galaxy, but their spectra vary with stellar mass, metallicity, gas mass fraction, formation history, and viewing angle. To account for these effects, we use averaged spectra over all galaxies with a stellar mass in the range $5.5 < \log(M_*/M_{\odot}) < 6.5$ and assume an average bolometric luminosity of $5 \times 10^{41} \text{ erg s}^{-1}$. This mass range is the best trade-off between the abundance and luminosity of high redshift galaxies: low-mass galaxies are more abundant and hence more typical at high redshift. However, the faintest galaxies are below the sensitivity threshold of *JWST* and despite their abundance they will not be the most frequently observed sources with *JWST*. Galaxies with $M_* \approx 10^6 M_{\odot}$ have a comoving number density of

$$\frac{dn}{d \log M_*} \approx 10^{-3} \text{ cMpc}^{-3} \quad (7)$$

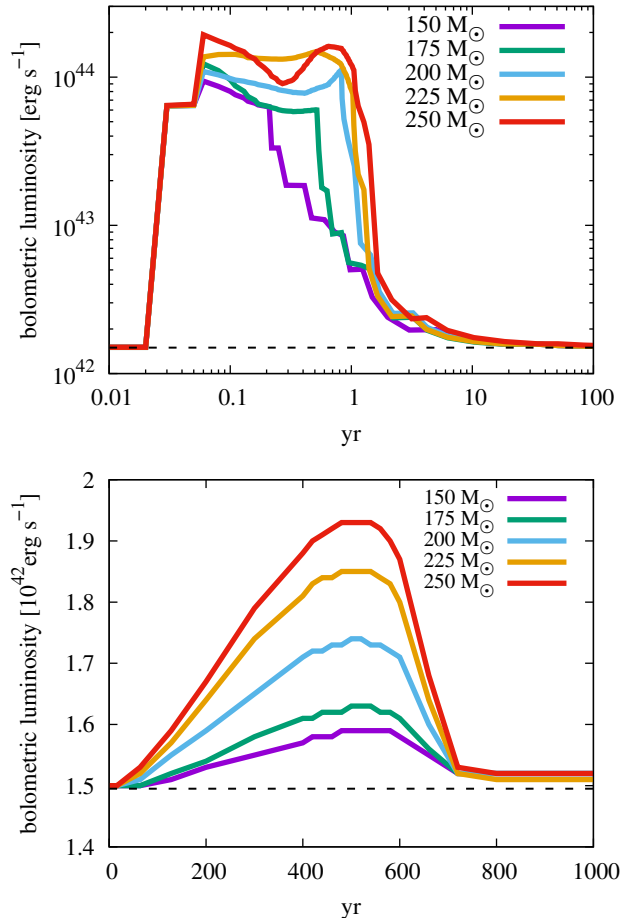


Figure 5. Bolometric light curves of the total emission after the explosion of PISNe of different progenitor masses. The time is source rest-frame and measured from when the first radiation escapes into the IGM. The inclusion of nebular emission (top) stretches the light curves to $\gtrsim 10 \text{ yr}$. The additional echo effect (bottom) smooths the light curves, which has two important consequences: the bolometric luminosity is fainter, but PISNe outshine the underlying stellar population for almost one thousand years, significantly longer than without this effect.

at redshift $z = 6$ (Barrow et al. 2017). The corresponding SED can be seen in Fig. 7. The SED of a typical, metal-enriched high redshift galaxy is close to the SED of our Pop III SSP with roughly the same luminosity. Due to the averaging over several galactic SEDs, their emission lines are not as prominent as for the Pop III SSP or the PISNe with nebular emission. Once we find a diagnostic to photometrically distinguish PISNe and the underlying Pop III SSP, we expect metal enriched galaxies not to compromise this diagnostic. We will discuss this distinction and the corresponding constraints more quantitatively in the next sections. For a more general discussion on the *JWST* signatures of high redshift galaxies, see Zackrisson et al. (2017).

3.2 Detection strategy for prompt emission

Many previous studies focused on the modelling and observational signatures of the prompt PISN emission (Scannapieco et al. 2005; Weinmann & Lilly 2005; Frost et al. 2009;

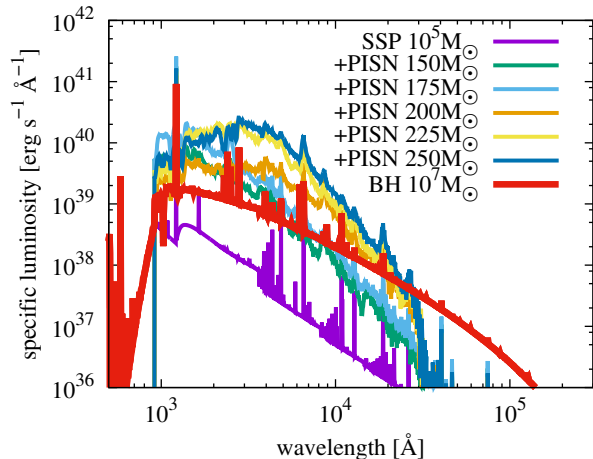


Figure 6. SEDs of a $10^7 M_{\odot}$ BH that accretes at 1% of its Eddington rate (red) compared to the average SEDs of PISNe of different progenitor mass. The BH SED peaks in the same wavelength range, but is broader than the PISN SEDs. All models include reprocessing of the radiation, either by the ISM or the BLR.

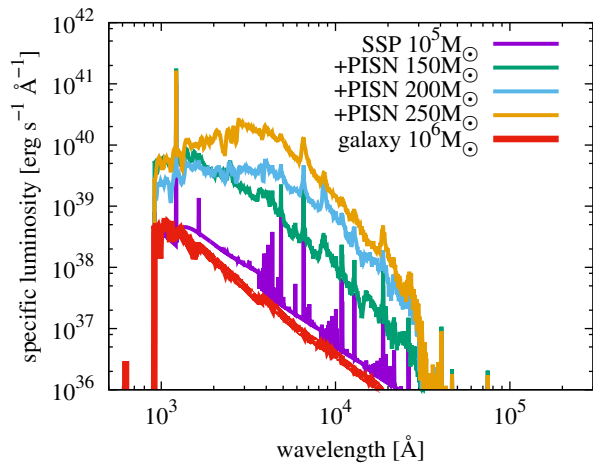


Figure 7. SEDs of the underlying SSP of Pop III stars, three PISNe of different progenitor masses and a typical high redshift metal enriched galaxy based on the model of Barrow et al. (2017). The SED of this metal enriched galaxy is very close to that of the Pop III stellar population. Here, nebular emission is included for a gas density of 100 cm^{-3} , which also prevents the escape of ionising radiation bluewards of 912 \AA .

Kasen et al. 2011; Pan et al. 2012; Hummel et al. 2012; Whalen et al. 2013; de Souza et al. 2013, 2014). In this section we present the photometric signature of PISNe and for the first time derive the optimal filter combination to detect their prompt emission and determine the most efficient exposure time and survey strategy.

The basic idea and strategy to detect PISNe at high redshift is as follows: PISNe are very bright over a period of roughly one year in the source rest frame. This time interval gets stretched to about one decade in the observer frame due to the cosmic expansion. If we could identify a PISN candidate in one observation, we can observe the same source a few months later to verify if it is a transient source, which would confirm the detection of a PISN. The crucial point

is to maximise the fraction of the lightcurve that we can observe, because the probability to find a PISN in the first place is directly proportional to the visibility time, t_{vis} , over which we can detect it.

In this section, we only focus on the prompt emission and do not account for the nebular emission or echo effect. We cut the SED below $\lambda < 912 \text{ \AA}$ to mimic the neutral IGM at high redshift, but this has only a minor influence on the calculated photometric fluxes. Due to the very faint fluxes, the wide band filters of JWST are the best choice for the photometric detection of PISNe. The expected light curves in the observer frame can be seen in Fig. 8. The flux increases with progenitor mass and with decreasing redshift. The time evolution of the flux is not monotonous with time and differs from filter to filter. The flux is very faint in the 070W and 090W filter, because we only have the direct prompt emission and no reprocessed recombination lines in this wavelength range. The filters with the highest expected signal-to-noise ratio (SNR) to detect PISNe are: F150W, F200W, F277W, F356W, F444W. The typical high- z galaxy and AGN yield fainter fluxes, although an AGN at $z \approx 6$ might have the same flux in certain filters as a PISN at $z \approx 12$.

We are interested in a reliable diagnostic to find PISN candidates that can then be further analysed for their transient nature. We want to maximise the observer frame time over which a PISN is detectable for a given diagnostic, because the probability to find a PISN is linearly proportional to this visibility time and since PISNe are very rare events (see Section 4.1), we need to identify an efficient filter combination. In the following sections we derive the optimal survey strategy by maximising the visibility time of the PISN lightcurve per exposure time invested. This visibility time depends on the selected filter, progenitor mass, redshift, and the desired signal-to-noise threshold. To calculate the visibility time, we define our standard sample of 5 PISNe ($150, 175, 200, 225, 250 M_{\odot}$) at 3 different redshifts ($z = 6, 9, 12$). We then identify the observer frame visibility of this ensemble of 15 PISNe as the cumulative time over which their prompt emission is detectable in a certain filter combination for a given exposure time. Our goal is to detect a PISN, irrespective of its progenitor mass or redshift and we hence aim at maximising the visibility time of this entire ensemble.

To better illustrate the physical meaning of this observability time, we also provide the corresponding fraction of the lightcurve that is observable. In the optimal case, we can observe 100% of the lightcurve, but as we will see below, this requires unnecessary long exposure times. This fraction of the lightcurve depends on our definition of the duration of the prompt emission. To simplify the comparison, we use the $250 M_{\odot}$ as standard scenario, which has a maximum visibility time of $\sim 340 \text{ d}$ in the source rest frame. All following fractional visibility times of the lightcurve are for a $250 M_{\odot}$ PISN, normalised to this value.

NIRCam on board *JWST* has a beam splitter that allows simultaneous observation of a source in one short wavelength and one long wavelength channel. In the following sections, we make use of this feature by combining two corresponding filters. The tabulated sensitivity f_{lim} of NIRCam is given at a SNR of $S/N = 10$ and for an exposure time of $t_{\text{exp}} = 10 \text{ ks}$. These values are for point sources and the

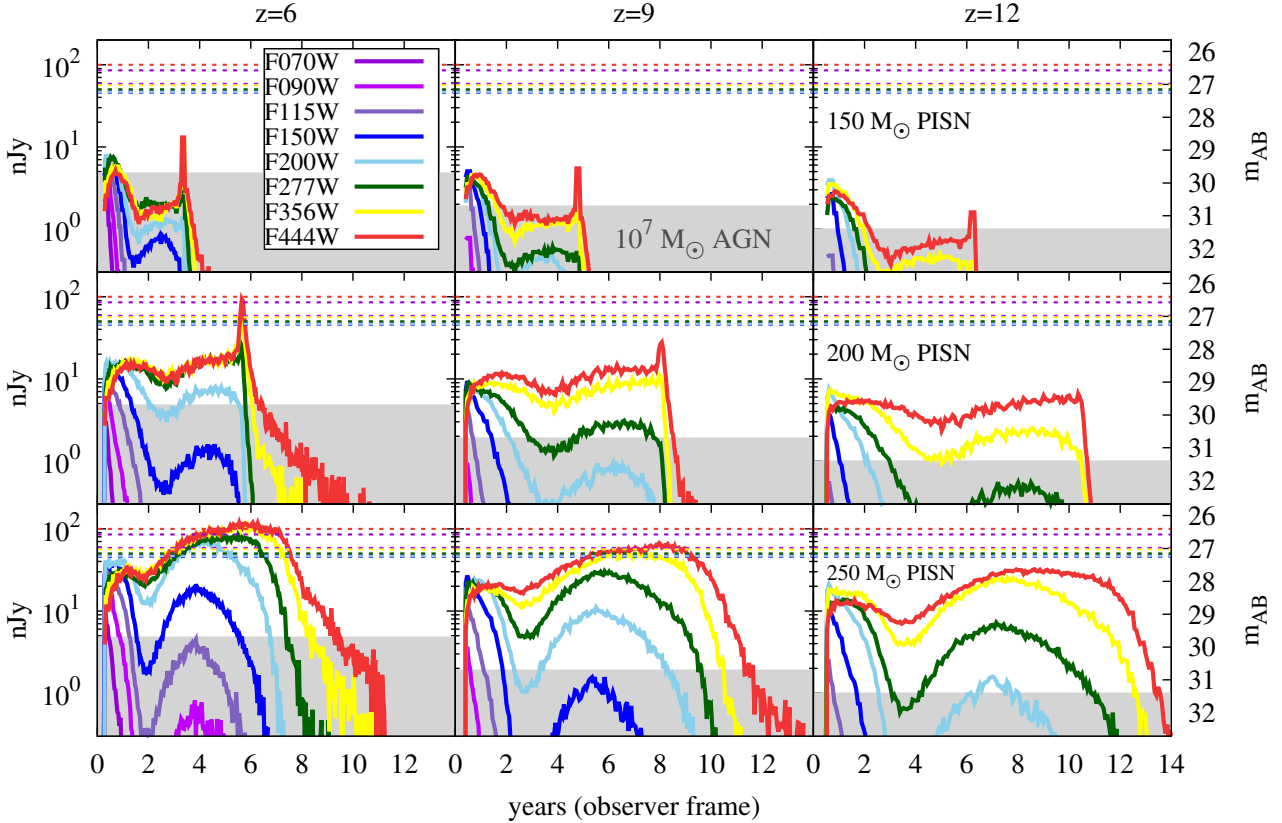


Figure 8. Lightcurves of the prompt PISN emission for three different progenitor masses (top: $150 M_{\odot}$, middle: $200 M_{\odot}$, bottom: $250 M_{\odot}$) at three different redshifts (left: $z = 6$, middle: $z = 9$, right: $z = 12$) in the *JWST* wide-band filters as a function of time in the observer-frame. The left vertical axis indicate the flux in nJy and the right axis yields the corresponding monochromatic AB-magnitude. The different filters are illustrated by the different colors and the corresponding sensitivity limit for a 600 s exposure are indicated by the horizontal dotted lines in each panel. The grey area indicates the expected flux from an AGN, powered by a $10^7 M_{\odot}$ BH. For simplicity we only plot the AGN flux in the 444W filter, which is the highest flux and hence represents a conservative upper limit.

actual signal-to-noise depends on the galactic foregrounds and therefore on the source position. Our derived exposure times at $S/N = 10$ should hence be treated as an optimistic lower limit. To convert the tabulated to an arbitrary exposure time, we assume the proportionality

$$f_{\text{lim}} \propto \frac{1}{\sqrt{t_{\text{exp}}}}, \quad (8)$$

and a linear response of the detector over its dynamical range.

3.2.1 2-filter diagnostic

The most efficient diagnostic is based on two filters that can be exposed simultaneously. In Fig. 9, we show one possible 2-filter diagnostic (which we demonstrate later to be the optimal filter combination) to illustrate the effect of a varying exposure time. As expected, the PISN visibility time increases with the exposure time. Already in a 450 s exposure we can identify the most luminous $225 M_{\odot}$ and $250 M_{\odot}$ PISN at $z = 6$ with $S/N > 10$. With a longer exposure time of $\gtrsim 10$ ks we could even detect the $200 M_{\odot}$ PISN at $z = 6$ and the $225 M_{\odot}$ out to $z = 12$. In order to not only maximise the PISN visibility, but to optimise the effort, we maximise the ratio of the visibility time to the exposure time to obtain the highest probability of finding PISNe per invested

exposure time. PISNe with $M < 200 M_{\odot}$ are not detectable with $S/N > 10$ for $t_{\text{exp}} \leq 10$ ks, but this does not affect the performance of the diagnostic. PISNe at higher redshift are favorable because their lightcurve gets stretched by a larger factor, which increases their observer frame visibility, but they are also significantly fainter. For different filter combinations and various exposure times we provide the cumulative observer frame visibility of the PISNe in Table 1. The visibility time for $t_{\text{exp}} \lesssim 10$ ks is dominated by the $225 M_{\odot}$ and $250 M_{\odot}$ PISNe at $z = 6$. We assume that all PISNe have the same probability to occur and that the rate of PISNe is constant in the redshift range $z = 6 - 9$, which agrees with Magg et al. (2016); however, see Hummel et al. (2012); Johnson et al. (2013). For a different IMF or PISN rate, one could weight the contributions to the rest frame visibility accordingly. Moreover, we do not explicitly take other sources into consideration, such as metal enriched galaxies or an AGN, because they are fainter than the prompt PISN emission and vary on much longer timescales than the PISN. The visibility fraction is an additional illustration to demonstrate the effect of a varying exposure time. This saturates for exposure times $\gtrsim 10$ ks and doubling the exposure time does not yield much more information.

We further quantify the ratio of the visibility to the exposure time in Fig. 10. We find a peak of the efficiency

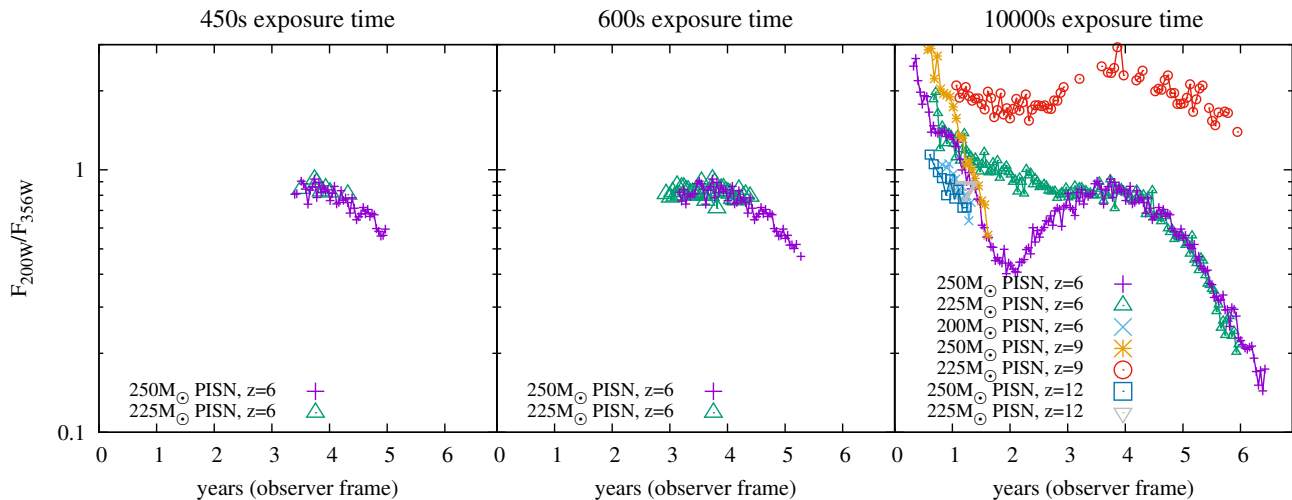


Figure 9. Most promising 2-filter diagnostic for different exposure times. The points illustrate the time evolution of the light curve (connected points are separated by 2 days in the source rest frame) for detections with signal-to-noise ratio $S/N > 10$ in both filters. With increasing exposure time, we can see the prompt emission over a longer time period. Exposure times of < 1 ks are sufficient to detect the brightest PISNe at $z = 6$, and for $t_{\text{exp}} \geq 10$ ks, PISNe at $z > 12$ are detectable.

t_{exp} [ks]	150W	150W	150W	200W	200W	200W
	-	150W	150W	-	-	-
	277W	356W	444W	277W	356W	444W
0.45	0	0	0	532	672	0
	(0%)	(0%)	(0%)	(22%)	(24%)	(0%)
0.54	0	0	0	700	1078	14
	(0%)	(0%)	(0%)	(26%)	(28%)	(1%)
0.6	0	0	0	994	1288	56
	(0%)	(0%)	(0%)	(29%)	(32%)	(1%)
0.72	0	0	0	1498	1526	322
	(0%)	(0%)	(0%)	(33%)	(34%)	(14%)
1.2	0	0	0	2268	2184	840
	(0%)	(0%)	(0%)	(44%)	(44%)	(34%)
3.6	1788	1540	826	3746	3458	2562
	(16%)	(12%)	(4%)	(77%)	(74%)	(57%)
5.4	2274	2070	1358	4276	3992	2940
	(31%)	(29%)	(16%)	(83%)	(81%)	(63%)
10	3216	2848	2156	6784	6434	4786
	(45%)	(45%)	(37%)	(94%)	(94%)	(86%)
100	7138	7188	5928	14608	14732	13326
	(73%)	(73%)	(72%)	(100%)	(100%)	(100%)

Table 1. Observer frame visibility in days for different 2-filter diagnostics and various exposure times. The percentage in parenthesis below each visibility time indicates the fraction of the lightcurve for the $250 M_{\odot}$ PISN at $z = 6$ that is visible for this exposure time.

for the filter combination 200W-356W at an exposure time of 600s. With this optimal combination of filters and exposure time we can detect roughly two days of the PISN lightcurves in the observer frame per one second of exposure time. The 200W-277W color has a comparable but slightly weaker performance, and for other filter combinations the most economic exposure time is $\gtrsim 1000$ s, but their overall performance is significantly smaller.

The filters 200W and 356W are in the short and long wavelength channel of NIRcam and can hence be used simultaneously. Our results imply that ten individual observations of different fields of view (FoV) with 600s exposure

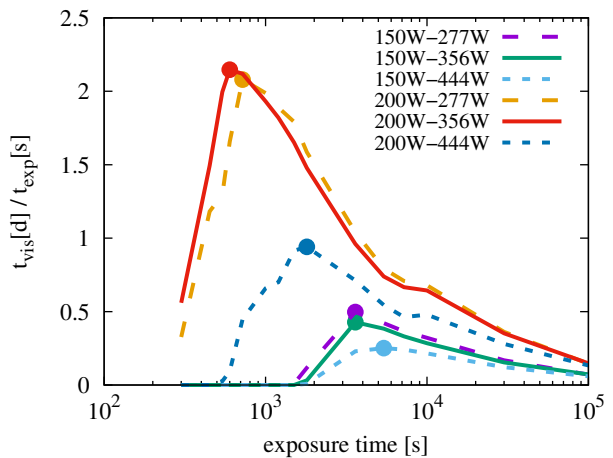


Figure 10. Efficiency of 2-filter combinations, quantified by the visibility time divided by the exposure time, as a function of the exposure time. This analysis illustrates that 200W-356W is the most promising filter combination with an optimal performance for an exposure time of 600 s. The 200W-277W color has a slightly weaker performance with almost the same optimal exposure time.

time each are more promising than one with an exposure time of 6000 s.

3.2.2 4-filter diagnostic

The identification of PISNe as transient sources poses two challenges: first, we have to identify them as promising candidates and second, we have to verify their transient nature and their unique colors in a follow-up observation. Although the PISN SED changes with time, some colors are constant over $\gtrsim 4$ yr (see Fig. 9), which makes it difficult to identify their transient nature with a two filter diagnostic. Moreover, we cannot account for all astrophysical sources that could have a similar photometric flux, and possibly even time evo-

t_{exp}	150W-277W	150W-356W	150W-277W
	vs. 200W-444W	vs. 200W-444W	vs. 200W-356W
2 ks	84 (0%)	84 (0%)	196 (1%)
3 ks	560 (1%)	560 (1%)	1330 (9%)
4 ks	952 (5%)	952 (5%)	1638 (16%)
6 ks	1498 (20%)	1498 (20%)	2242 (32%)
20 ks	3062 (64%)	3062 (64%)	4010 (54%)
100 ks	5928 (72%)	5928 (72%)	7066 (73%)

Table 2. Observer frame visibility in days for different color-color diagnostics and various exposure times. The values are stable under permutation of the four filters, as long as the long wavelength channel is subtracted from the short wavelength channel. The percentage in parenthesis indicates the fraction of the lightcurve for the $250 M_{\odot}$ PISN at $z = 6$ that is visible for this exposure time.

lution, as the PISN. Therefore, we also provide a color-color diagnostic based on 4 filters, which solves these problems: the 4-filter diagnostic shows a more reliable time evolution of the colors and it helps to better distinguish the PISN from other sources and hence permits a more precise identification. We show the most promising color-color diagrams for different exposure times in Fig. 11. We proceed in the same way as for the 2-filter diagnostic and present the observer frame visibility times in Table 2. Since we require that the PISN has to be detected in 4 filters simultaneously at $S/N > 10$, the visibility time is shorter than in the 2-filter diagnostic. By maximising the ratio of visibility time to exposure time we determine the optimal filter combination and corresponding exposure time (see Fig. 12). We find a peak of the efficiency for the two color combination 150W-277W vs. 200W-356W at an exposure time of 3 ks. With this optimal combination of filters and exposure time we can detect ~ 11 h of the PISN lightcurves in the observer frame per one second of exposure time. Note that the stated exposure times are for one filter only. If the short and long wavelength channel are used at the same time, the stated exposure times have to be multiplied by two for the overall exposure time for this 4-filter diagnostic.

3.2.3 Only $z \geq 9$ PISNe

Our previous estimates depend on the assumptions that the probability of a PISN explosion is independent of the redshift in the range $6 \leq z \leq 12$. Whereas Magg et al. (2016) find an almost constant rate of PISNe between $z = 20$ and $z = 6$, Hummel et al. (2012) and Johnson et al. (2013) report a steep decrease in the PISN rate after $z \approx 10$ with almost no PISN at $z = 6$. The rate of PISNe is to first order proportional to the star formation rate of Pop III stars and both are strongly suppressed at lower redshift by radiative and chemical feedback. Under the assumptions that no PISNe explode at $z < 9$, we derive the optimal diagnostic to identify PISN at $z \geq 9$. We use the same standard set of PISN with 5 different progenitor masses as before, but now consider only the redshifts $z = 9$ and $z = 12$. The time evolution of the most promising 2-filter diagnostic is given in Fig. 13. This restriction to PISN at higher redshift increases the required exposure times to > 6 ks. The $250 M_{\odot}$ PISN is faint between 2 and 4 yr in the observer frame, which renders the $225 M_{\odot}$ PISN at $z = 9$ the dominant contribution

t_{exp}	150W	150W	150W	200W	200W	200W
	- 277W	- 356W	- 444W	- 277W	- 356W	- 444W
6 ks	200 (5%)	100 (3%)	0 (0%)	520 (11%)	432 (7%)	0 (0%)
10 ks	486 (8%)	286 (6%)	0 (0%)	2220 (14%)	2066 (12%)	1020 (0%)
12 ks	606 (9%)	406 (8%)	0 (0%)	2766 (15%)	2710 (14%)	1640 (1%)
15 ks	792 (9%)	612 (9%)	80 (1%)	3204 (22%)	3266 (21%)	2200 (12%)
30 ks	1336 (11%)	1036 (11%)	660 (9%)	5036 (43%)	4852 (43%)	3460 (41%)
100 ks	2658 (14%)	2610 (14%)	1938 (14%)	7566 (60%)	7564 (60%)	6494 (59%)

Table 3. Observer frame visibility of PISNe at $z \geq 9$ in days for different 2-filter diagnostics and various exposure times. The percentage in parenthesis below each visibility time indicates the fraction of the lightcurve for the $250 M_{\odot}$ PISN at $z = 9$ that is visible for this exposure time.

for the optimal exposure time of 3 ks. The steady change of the 200W/277W color with time after explosion makes it easy to detect these PISNe as transient sources. The visibility time of these PISNe in the observer frame are given in Table 3. Even for very long exposure times the visible fraction of the lightcurve of $z > 9$ PISNe remains below $\sim 60\%$. In Fig. 14 we show the efficiency of these filter diagnostics and derive the optimal exposure time. The combination of the 200W and 277W filters is the best choice to detect PISNe at $z \geq 9$ with an optimal exposure time of 12 ks.

3.3 Detecting the afterglow

We show the most promising 4-filter combinations to detect the PISN afterglow for an ISM density of $n_{\text{H}} = 100 \text{ cm}^{-3}$ in Fig. 15. Evidently, the unique identification of a PISN afterglow is beyond the capabilities of *JWST*, because it is too faint to be distinguished from the underlying stellar population. We still wish to outline a possible strategy for detection, with even more powerful telescopes in the future.

The most promising diagnostic is $F_{115\text{W}} - F_{444\text{W}}$, because it offers the largest range in which we only expect PISNe (green area). For the $F_{115\text{W}} - F_{277\text{W}}$ color, e.g., the $z = 12$ AGN is unfavourably close to the PISN signature, which would require an even higher sensitivity to distinguish them. The $F_{090\text{W}} - F_{277\text{W}}$ color on the horizontal axis cannot be used to discriminate the PISNe from other sources, because the evolution of the squares with redshift has to be seen as a continuous time sequence (gray dotted line). The color of a Pop III population at $z = 7$ will be between the values of $z = 6$ and $z = 9$, which prevents a unique identification around $F_{090\text{W}} - F_{277\text{W}} \approx 0.1 \text{ nJy}$. However, this color could be used as an additional constraint.

For the $F_{115\text{W}} - F_{444\text{W}}$ combination (see detailed time evolution in Fig. 16), we need a sensitivity of at least 0.2 nJy in both filters to discriminate the $250 M_{\odot}$ PISN 300-600 yr after its explosion from the underlying stellar population at $S/N > 10$. This requires an exposure time of $1.5 \times 10^8 \text{ s} \approx 5 \text{ yr}$, far beyond the capabilities of *JWST*. The remarkably long visibility time of $\sim 300 \text{ yr}$ in the source rest frame would be stretched by the cosmic expansion to over

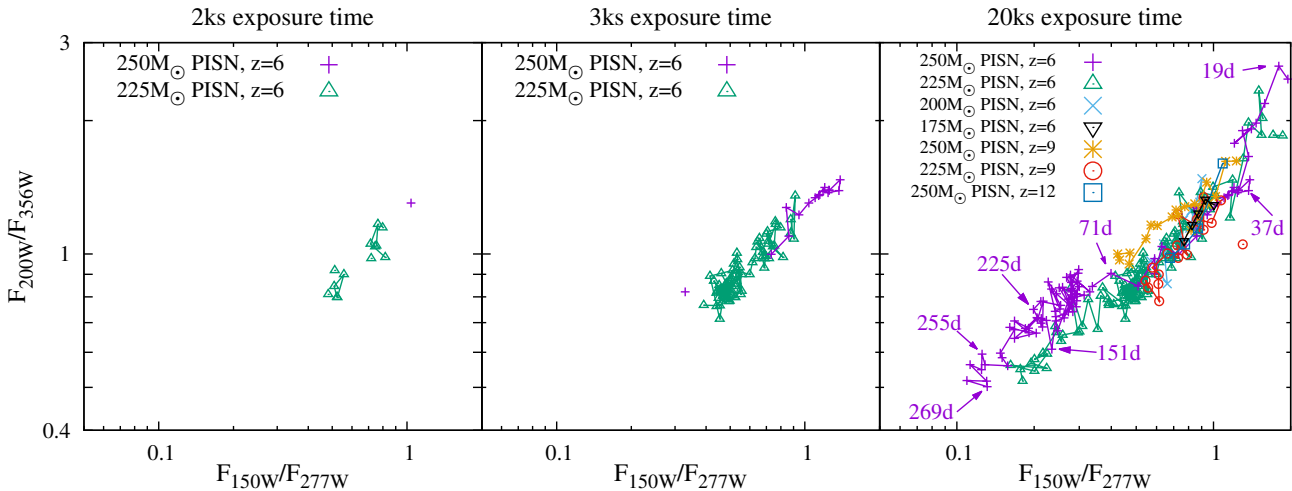


Figure 11. Most promising 2-color diagnostic for different exposure times. The points illustrate the time evolution of the light curve (connected points are separated by 2 days in the source rest frame) for detections at $S/N > 10$ in all four filters. In the right panel we explicitly show the time evolution by indicating the days in the source rest frame after explosion. With increasing exposure time we can detect the prompt emission for longer and for $t_{\text{exp}} \gtrsim 20$ ks, the $175 M_{\odot}$ PISN at $z = 6$ and the $250 M_{\odot}$ PISN at $z = 12$ are observable.

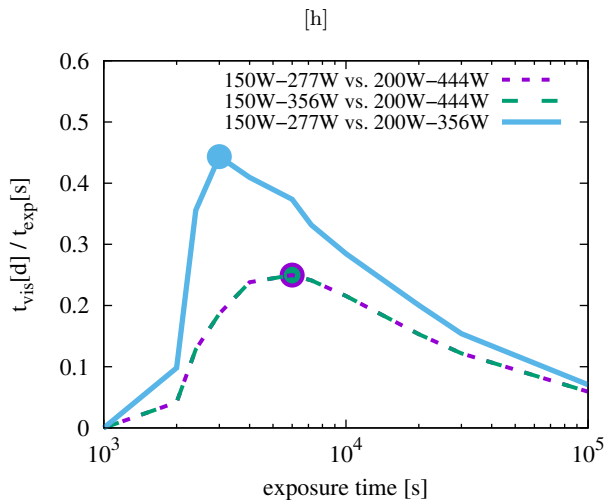


Figure 12. Efficiency of 2-color diagnostics, measured by the visibility time divided by the exposure time, as a function of the exposure time. This analysis illustrates that the 2-color diagnostic 150W-277W vs. 200W-356W is the most promising filter combination with an optimal performance for an exposure time of 3 ks. For other filter combinations including 444W the most economic exposure time is 6 ks, but the overall performance is smaller than for the optimal filter combination.

2000 yr. However, this yields an efficiency of only 7 min of visibility per 1 s invested exposure time and is hence significantly less economical than the detection of the direct PISN emission. Moreover, not every Pop III hosting halo is expected to exhibit high enough densities to maintain neutral gas and create this afterglow.

This derivation is not intended to guide blind deep field surveys to detect and identify the PISN afterglow. We rather want to illustrate the typical color evolution of such a PISN afterglow, discuss the typical timescales, and highlight which other sources could mimic such a photometric signature. The unique identification of the PISN afterglow is beyond the ca-

capabilities of *JWST*, but these results are relevant for possible future observations: after the detection of prompt PISN emission, our model predicts the expected afterglow signature, depending on the ISM properties. Hence, the PISN afterglow can be used to probe the ISM at high redshift. Moreover, the detection rates of the PISN afterglow are more than two orders of magnitude higher than for the prompt emission, because the lightcurve gets stretched by the nebular emission and the echo effect.

4 SURVEY STRATEGIES

To determine the optimal survey strategy for PISNe, we first have to assess their detection rates. Succinctly put: Do we expect to find one PISN, or one thousand events over the mission time of *JWST*?

4.1 Detection Rates

With our optimised 2-filter detection strategy (200W-356W, 600 s exposure) *JWST* can detect PISNe of progenitor masses $225 M_{\odot}$ and $250 M_{\odot}$ out to redshift $z \sim 7.5$. For a $250 M_{\odot}$ PISN we can see 32% of the lightcurve ($S/N > 10$ in both filters), which directly translates into the probability of observing the PISN at the right moment. For a $225 M_{\odot}$ PISN we can detect 22% of the lightcurve. Assuming a logarithmically flat IMF in the PISN mass range ($140 - 260 M_{\odot}$), the $225 M_{\odot}$ and $250 M_{\odot}$ PISNe probe together 33% of the PISN mass range. In Table 4, we list different PISN rates from the literature. Whereas the different models yield PISN rates, which differ by almost 2 orders of magnitude at $z = 6$, they all agree on the expected rates for PISNe from $z \approx 9$. If we assume the optimistic rate for $z < 7.5$ by Magg et al. (2016), and multiply it with the fraction of the PISN progenitor mass range that is observable and with the probability that we see the PISN lightcurve at the right time, the de-

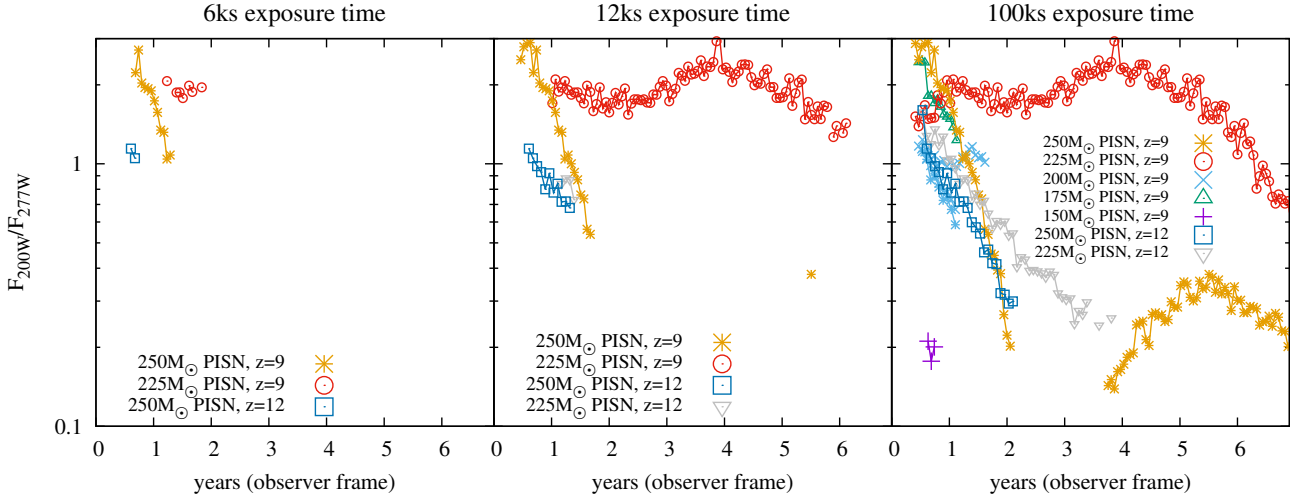


Figure 13. Most promising 2-filter diagnostic for different exposure times for PISN at $z \geq 9$. The points illustrate the time evolution of the light curve (connected points are separated by 2 days in the source rest frame) for detections at $S/N > 10$ in both filters. For the optimal exposure time of 12 ks ≈ 200 min, we can even detect all PISNe at $z = 9$ and $225 M_{\odot}$ PISNe out to $z = 12$. Longer exposures than this optimal value do not yield a larger fraction of the PISN lightcurve.

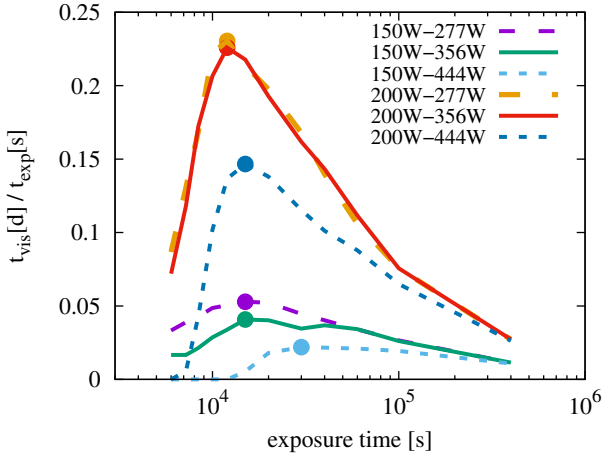


Figure 14. Efficiency of given filter combination, measured by the visibility time divided by the exposure time, as a function of the exposure time for PISNe at $z \geq 9$. The F200W-F277W is the most promising diagnostic with an optimal exposure time of 12 ks.

	$z \leq 7.5$	$7.5 < z \leq 12$
Hummel et al. (2012)	$6 \times 10^{-6}/\text{yr}/\text{FoV}$	$7 \times 10^{-4}/\text{yr}/\text{FoV}$
Johnson et al. (2013)	$5 \times 10^{-5}/\text{yr}/\text{FoV}$	$3 \times 10^{-4}/\text{yr}/\text{FoV}$
Magg et al. (2016)	$2 \times 10^{-4}/\text{yr}/\text{FoV}$	$4 \times 10^{-4}/\text{yr}/\text{FoV}$

Table 4. PISN rates per year per *JWST* field of view (FoV, $2.2' \times 2.2'$). They roughly agree at $z > 7.5$, but differ by almost two orders of magnitude at lower redshift.

tection rate for PISNe with *JWST* is

$$R_{600s} = 2 \times 10^{-5} \text{ yr}^{-1} \text{ FoV}^{-1}. \quad (9)$$

Phrased differently, with the optimal survey strategy, *JWST* will be able to detect one PISN per year per $\sim 50,000$ different exposures of 600s each. In the more conservative case, where we do not expect PISNe at $z \leq 7.5$, the detection

rate will be $(2.7 \pm 0.4) \times 10^{-5} \text{ yr}^{-1} \text{ FoV}^{-1}$, but for a longer exposure time of 12 ks for each individual FoV. This detection rate is in agreement with the mean and variance of the models by Hummel et al. (2012); Johnson et al. (2013); Magg et al. (2016).

The observed detection rates are proportional to the star formation efficiency of Pop III stars and directly linked to the range and shape of their IMF. The detection rates of first SNe with *JWST* will therefore help to reveal the nature of the first stars and even their non-detection can be used to constrain the Pop III IMF.

4.2 Optimal Survey Strategies

PISNe are rare events and a total exposure time of 3×10^7 s, distributed over 50,000 FoVs, is needed to detect at least one event. It is evident that a blind survey, only dedicated to find such PISNe from the first stars, is not feasible. We therefore present other observational strategies and approaches to detect the first SNe with *JWST*.

We should make use of archival data to select promising targets for follow-up observations. The most unique feature of PISNe is not their extreme luminosity or their specific color, but rather their transient nature and the shape of their lightcurve (Pan et al. 2012). The identification of a PISN candidate and a well-targeted follow-up observation of this source will be one of the most promising paths to identify the first SNe. With the right filter combinations, there should be about one candidate in every 50,000 *JWST* FoVs. If efficiently done, such an archival strategy should be able to detect of order 10 PISNe during its (~ 10 yr) mission lifetime.

To make this strategy successful, we highlight the optimal filter combinations to identify PISNe. Independent of their redshift distribution, we find the F200W filter to be the optimal choice in the short wavelength channel and the F356W (F277W) filter in the long wavelength channel for PISNe below (above) $z \approx 7.5$. These filters are also re-

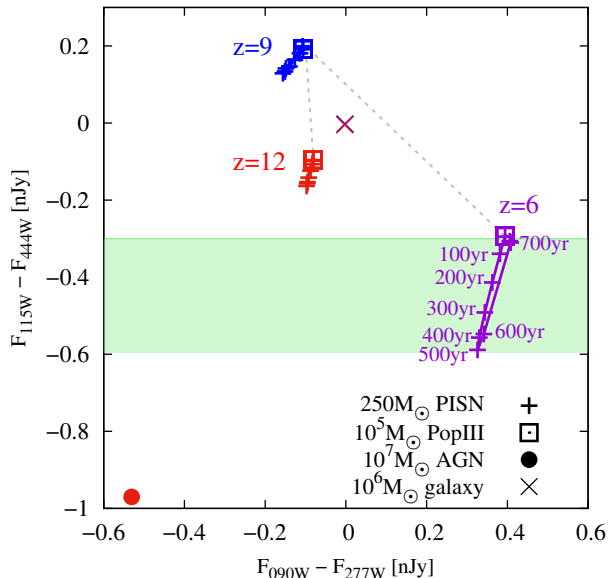


Figure 15. Color-color diagnostics to best distinguish PISNe with nebular emission and the echo effect from other high-redshift sources. The three colors illustrate different redshifts and the pluses indicate the time evolution of a $250 M_{\odot}$ PISN. Explosions with smaller masses cannot be distinguished from the underlying population of Pop III stars (squares). The typical high redshift galaxy (crosses) is very faint and the AGN (filled circle) is so bright that only its $z = 12$ realisation falls in the relevant color range. In the green range we expect only PISNe: for redder colors the high-redshift AGN falls in the same spectral range and for bluer colors, the underlying populations prevents a unique identification (the gray dotted line illustrates the expected smooth color transition with redshift).

quired in the most promising 4-filter diagnostics. All blind observations with $t_{\text{exp}} \gtrsim 600$ s, employing these filters, will help in selecting PISN candidates for follow up. The latter could be performed with *JWST*, or with next-generation ground-based telescopes such as the Giant Magellan Telescope (GMT), or the European Extremely Large Telescope (E-ELT). A main advantage of the first SNe is their cosmologically dilated lightcurve, which makes them observable in follow-ups for over 10 years. Other observational facilities, such as WFIRST, LSST, and Pan-STARRS will complement the search for the first SNe (Young et al. 2008; Whalen et al. 2013; Tanaka et al. 2013; Smidt et al. 2015).

The optimal exposure time to detect PISNe is $t_{\text{exp}} = 600$ s, which is of the same order as the overhead of ~ 280 s for the guide star acquisition after pointing to a new target. For the necessary $\sim 50,000$ individual FoVs, the overhead would sum up to an unnecessary long amount of unused time. We hence rather suggest to include a 600 s exposure with the optimal filters F200W and F356W, every time that *JWST* points towards a new blind field.

A lower threshold of $S/N > 5$, instead of $S/N > 10$, yields shorter optimal exposure times and hence a higher probability of identifying PISNe. Especially when it comes to searching the archival data for PISN candidates, the desired signal-to-noise ratio can be lowered to identify more interesting candidates for follow-up observations. Also strong grav-

itational lensing by massive galaxies and galaxy clusters at lower redshift could boost the flux from the first SNe and therefore increase their detection rates (Rydberg et al. 2013; Whalen et al. 2013).

The afterglow of a PISN is fainter than the prompt emission, but under optimistic conditions still within the capabilities of *JWST*. However, distinguishing the PISN afterglow from other sources requires sub-nJy sensitivities, which will not be feasible with *JWST*. The more reliable and realistic confirmation of the afterglow is its transient nature on timescales of several hundred years. We can create catalogs of PISNe and their candidates and monitor them over the next decades and even centuries, similar to follow-up studies of historical SN events (Somers et al. 1997; Shara et al. 2012; Miszalski et al. 2016; Shara et al. 2017). As is the case for GRBs (Gehrels et al. 2009), this opens a novel and unique technique to study the host environments of the first stars.

4.3 Existing Observations

Mould et al. (2017) present the observation of a $z = 6$ SLSN. They report the detection of a transient with $i = 25.19$, $z = 24.97$, and $Y = 25.0$ in 2016, significantly brighter than in earlier observations 2013-2015. This transient source coincides with a possible host galaxy at the same sky position and redshift, identified by its Ly- α break between the i and z filter, which supports the interpretation as a $z = 6$ SLSN. They rule out other transient sources such as optically variable AGNs, Galactic halo flare stars, or a Type Ia SN at lower redshift. However, they cannot photometrically exclude a tidal disruption event. They estimate the frequency of SLSNe to be $\sim 6 \text{ yr}^{-1} \text{ deg}^{-2}$, but the expected rates of PISNe around $z = 6$ are significantly below their estimate (Hummel et al. 2012; Johnson et al. 2013; Magg et al. 2016), which would make it a very fortunate PISN detection. Also Pan et al. (2017) recently present the spectroscopic confirmation of a SLSN at $z = 1.9$, which they classify as a Type I SLSN. Another SLSN was observed in the spiral galaxy NGC 3191 (Chen et al. 2017). However, the solar-metallicity environment of this event excludes a Pop III event (Yusof et al. 2013).

None of the detected SLSNe sit comfortable within the model predictions for PISNe, and alternative mechanisms for these class of SLSNe are advocated and debated (Dessart et al. 2012; Nicholl et al. 2013; Lunnan et al. 2017; De Cia et al. 2017). The late-time decay of the lightcurve of several SLSNe, which is also characteristic for PISNe, could alternatively be powered by the spin-down of a newly-born magnetar (Inserra et al. 2013). This ambiguity further complicates the identification of PISNe, but the lack of metal lines at early times could provide a spectroscopic signature for identification (Hummel et al. 2012).

4.4 Caveats

Our model is based on several assumptions and approximations that we want to critically discuss.

The PISN lightcurves employed here are based on the model by Kasen et al. (2011), although there are other models, which yield different predictions for the spectral time evolution (Scannapieco et al. 2005; Woosley et al. 2007; Pan

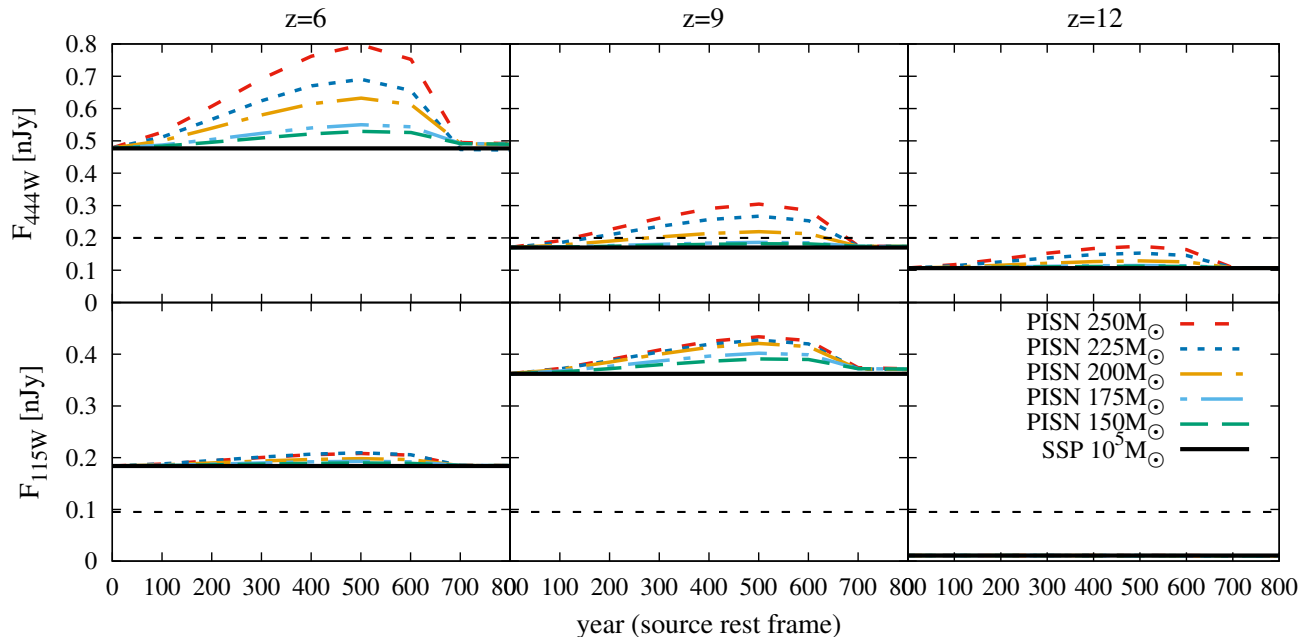


Figure 16. Time evolution of the flux in the two most promising filters for the PISN afterglow. The time is in the source rest frame, and the time of observability will be stretched by about one order of magnitude. The horizontal dashed line indicates the sensitivity limit for an exposure time of 1.5×10^8 s, necessary to distinguish the PISN from the underlying stellar population. The flux in F115W increases between $z = 6$ and $z = 9$, because the Ly α line gets shifted into this filter.

et al. 2012; Chen et al. 2014; Jerkstrand et al. 2016; Kozyreva et al. 2017; Gilmer et al. 2017). A quantitative comparison of the different models is beyond the scope of this paper, but our photometric signatures may be affected by our specific choice. Our optimal survey strategy targets the remnants of Pop III stars with masses above $200 M_{\odot}$. Their existence is not yet confirmed and simulations of primordial star formation tend to predict lower typical masses for the first stars (Stacy et al. 2010; Hirano & Bromm 2017). However, the possible non-detection of PISNe over the next decade would not exclude their existence, because Pop III stars below $200 M_{\odot}$ could also yield PISNe, but they might be below our detection limits.

We have included several high-redshift sources that could mimic a PISN, but we cannot exclude all possible objects. Especially tidal disruption events of stars in the strong tidal field near a supermassive black hole have a similar signature and transient nature as a SLSN (Leloudas et al. 2016; Holoiën et al. 2016), and it is difficult to distinguish them photometrically. In addition, Milky Way M-dwarfs could have a similar red spectrum and their proper motion could mimic an intrinsic variability if they disappear at their location in a follow-up survey. A comprehensive analysis of possible local, photometrically similar, sources needs to be carried out in future work.

Although the a-posteriori treatment of the resonant Ly α scattering does not change the photometric signature of the afterglow, it affects its time evolution: the path of Ly α photons is longer due to multiple scatterings, and our predicted time over which we smooth the emission gets also stretched. A self-consistent radiative transfer calculation is better suited to correctly predict the photometric time evolution of the afterglow signature. Also the ISM substructure

and SNe that explode off the halo center will alter the reprocessing of the radiation. Although these effects are crucial for a proper characterization of the afterglow, the reprocessed radiation is below the detection limit of *JWST*, and only prompt emission will be observable, if at all.

5 SUMMARY AND CONCLUSIONS

We determined the photometric signature of PISNe and derive the optimal filter combination and survey strategy for their detection with *JWST*: a blind field observation with the two wide-band filters F200W and F356W, together with an exposure time of $t_{\text{exp}} = 600$ s, maximize the visibility time per invested exposure time. The goal is to analyze 50,000 different FoVs to select promising PISN candidates that can be further analyzed with follow-up observations for their transient nature. With this optimal survey strategy one can identify a single PISN per year, which would mark a milestone in the study of the first stars as their first direct detection.

In parallel to high redshift gamma-ray bursts (Ciardi & Loeb 2000; Gehrels et al. 2009), PISNe will also help us to probe their host environment and the pre-reionisation intergalactic medium (IGM) via their afterglow emission. The time evolution of the afterglow is sensitive to the density and radius of the ISM, with the change in magnitude revealing the ionisation state of the gas and hence the emissivity of ionising photons of the underlying stellar population, and the absorption spectroscopy probing properties of the IGM.

The planned launch of *JWST* in 2019, together with complementary facilities such as WFIRST or the LSST, will enable the detection of the first SNe, thus ushering in the

epoch of direct detections of the first stars. Our novel approach to determine the optimal filter combination and exposure time can also be applied to other surveys to maximize their success. The transient Universe at high redshifts is about to provide an exciting new window into the end of the cosmic dark ages.

Acknowledgements

The authors thank Kirk Barrow for providing his SEDs of high- z galaxies, Mattis Magg for sharing his PISN rates, and Dan Kasen for the availability of his PISN SEDs. We appreciate valuable discussions with Caterina Umilta, Alba Vidal Garcia, Simon Glover, and Eric Pellegrini. TH acknowledges funding under the European Community's Seventh Framework Programme (FP7/2007-2013) via the European Research Council (ERC) Grant 'BLACK', under the project number 614199. VB was supported by NSF grant AST-1413501. AL was supported in part by the Black Hole Initiative at Harvard University, which is funded by a grant from the John Templeton Foundation. Calculations were performed with version 13.04 of CLOUDY, last described by Ferland et al. (2013).

REFERENCES

- Abbott T., Cooke J., Curtin C., Joudaki S., Katsianis A., Koekemoer A., Mould J., Tesfari E., Uddin S., Wang L., 2017, Publications of the Astronomical Society of Australia, 34, e012
- Abel T., Bryan G. L., Norman M. L., 2002, *Science*, 295, 93
- Aoki W., Tominaga N., Beers T. C., Honda S., Lee Y. S., 2014, *Science*, 345, 912
- Barkat Z., Rakavy G., Sack N., 1967, *Physical Review Letters*, 18, 379
- Barrow K. S. S., Wise J. H., Norman M. L., O'Shea B. W., Xu H., 2017, *MNRAS*, 469, 4863
- Bond J. R., Arnett W. D., Carr B. J., 1984, *ApJ*, 280, 825
- Bromm V., Coppi P. S., Larson R. B., 1999, *ApJ*, 527, L5
- Bromm V., Kudritzki R. P., Loeb A., 2001, *ApJ*, 552, 464
- Bromm V., Loeb A., 2003, *ApJ*, 596, 34
- Chandra P., Frail D. A., Fox D., Kulkarni S., Berger E., Cenko S. B., Bock D. C.-J., Harrison F., Kasliwal M., 2010, *ApJ*, 712, L31
- Chatzopoulos E., Wheeler J. C., 2012, *ApJ*, 748, 42
- Chen K.-J., Heger A., Woosley S., Almgren A., Whalen D. J., 2014, *ApJ*, 792, 44
- Chen T.-W., Schady P., Xiao L., Eldridge J. J., Schweyer T., Lee C.-H., Yu P.-C., Smartt S. J., Inserra C., 2017, *ApJ*, 849, L4
- Ciardi B., Loeb A., 2000, *ApJ*, 540, 687
- Clark P. C., Glover S. C. O., Smith R. J., Greif T. H., Klessen R. S., Bromm V., 2011, *Science*, 331, 1040
- Cooke J., Sullivan M., Gal-Yam A., Barton E. J., Carlberg R. G., Ryan-Weber E. V., Horst C., Omori Y., Díaz C. G., 2012, *Nature*, 491, 228
- de Bressan A., Salvadori S., Schneider R., Valiante R., Omukai K., 2017, *MNRAS*, 465, 926
- De Cia A., et al., 2017, arXiv:1708.01623
- de Souza R. S., Ishida E. E. O., Johnson J. L., Whalen D. J., Mesinger A., 2013, *MNRAS*, 436, 1555
- de Souza R. S., Ishida E. E. O., Whalen D. J., Johnson J. L., Ferrara A., 2014, *MNRAS*, 442, 1640
- Dessart L., Hillier D. J., Waldman R., Livne E., Blondin S., 2012, *MNRAS*, 426, L76
- Dijkstra M., Haiman Z., Spaans M., 2006, *ApJ*, 649, 14
- Dopcke G., Glover S. C. O., Clark P. C., Klessen R. S., 2013, *ApJ*, 766, 103
- Draine B. T., 2011, *Physics of the Interstellar and Inter-galactic Medium*
- Ferland G. J., Porter R. L., van Hoof P. A. M., Williams R. J. R., Abel N. P., Lykins M. L., Shaw G., Henney W. J., Stancil P. C., 2013, *RMxAA*, 49, 137
- Fraley G. S., 1968, *Astrophysics and Space Science*, 2, 96
- Frost M. I., Surace J., Moustakas L. A., Krick J., 2009, *ApJ*, 698, L68
- Fryer C. L., Woosley S. E., Heger A., 2001, *ApJ*, 550, 372
- Gal-Yam A., 2012, *Science*, 337, 927
- Gehrels N., Ramirez-Ruiz E., Fox D. B., 2009, *ARA&A*, 47, 567
- Gilmer M. S., Kozyreva A., Hirschi R., Fröhlich C., Yusof N., 2017, *ApJ*, 846, 100
- Greif T. H., Springel V., White S. D. M., Glover S. C. O., Clark P. C., Smith R. J., Klessen R. S., Bromm V., 2011, *ApJ*, 737, 75
- Habouzit M., Volonteri M., Latif M., Dubois Y., Peirani S., 2016, *MNRAS*, 463, 529
- Hartwig T., Bromm V., Klessen R. S., Glover S. C. O., 2015, *MNRAS*, 447, 3892
- Heger A., Woosley S. E., 2002, *ApJ*, 567, 532
- Hirano S., Bromm V., 2017, *MNRAS*, 470, 898
- Hirano S., Hosokawa T., Yoshida N., Umeda H., Omukai K., Chiaki G., Yorke H. W., 2014, *ApJ*, 781, 60
- Holoien T. W.-S., et al., 2016, *MNRAS*, 463, 3813
- Hosokawa T., Omukai K., Yoshida N., Yorke H. W., 2011, *Science*, 334, 1250
- Hummel J. A., Pawlik A. H., Milosavljević M., Bromm V., 2012, *ApJ*, 755, 72
- Inserra C., et al., 2013, *ApJ*, 770, 128
- Jerkstrand A., Smartt S. J., Heger A., 2016, *MNRAS*, 455, 3207
- Johnson J. L., Dalla Vecchia C., Khochfar S., 2013, *MNRAS*, 428, 1857
- Kasen D., Woosley S. E., Heger A., 2011, *ApJ*, 734, 102
- Kozyreva A., Gilmer M., Hirschi R., Fröhlich C., Blinnikov S., Wollaeger R. T., Noebauer U. M., van Rossum D. R., Heger A., Even W. P., Waldman R., Tolstov A., Chatzopoulos E., Sorokina E., 2017, *MNRAS*, 464, 2854
- Leloudas G., et al., 2016, *Nature Astronomy*, 1, 0002
- Lunnan R., et al., 2017, arXiv:1708.01619
- Mackey J., Bromm V., Hernquist L., 2003, *ApJ*, 586, 1
- Magg M., Hartwig T., Glover S. C. O., Klessen R. S., Whalen D. J., 2016, *MNRAS*, 462, 3591
- Miralda-Escudé J., Rees M. J., 1997, *ApJ*, 478, L57
- Miszalski B., Woudt P. A., Littlefair S. P., Warner B., Boffin H. M. J., Corradi R. L. M., Jones D., Motsoaledi M., Rodríguez-Gil P., Sabin L., Santander-García M., 2016, *MNRAS*, 456, 633
- Moriya T., Tominaga N., Tanaka M., Maeda K., Nomoto K., 2010, *ApJ*, 717, L83
- Mould J., Abbott T., Cooke J., Curtin C., Katsianis A.,

- Koekemoer A., Tescari E., Uddin S., Wang L., Wyithe S., 2017, arXiv:1704.05967
- Natarajan P., Pacucci F., Ferrara A., Agarwal B., Ricarte A., Zackrisson E., Cappelluti N., 2017, *ApJ*, 838, 117
- Nicholl M., et al., 2013, *Nature*, 502, 346
- Pacucci F., Ferrara A., Grazian A., Fiore F., Giallongo E., Puccetti S., 2016, *MNRAS*, 459, 1432
- Pan T., Kasen D., Loeb A., 2012, *MNRAS*, 422, 2701
- Pan T., Loeb A., 2013, *MNRAS*, 435, L33
- Pan Y.-C., et al., 2017, *MNRAS*, 470, 4241
- Planck Collaboration Ade P. A. R., Aghanim N., Arnaud M., Ashdown M., Aumont J., Baccigalupi C., Banday A. J., Barreiro R. B., Bartlett J. G., et al. 2016, *A&A*, 594, A13
- Rakavy G., Shaviv G., 1967, *ApJ*, 148, 803
- Rydberg C.-E., Zackrisson E., Lundqvist P., Scott P., 2013, *MNRAS*, 429, 3658
- Santos M. R., Bromm V., Kamionkowski M., 2002, *MNRAS*, 336, 1082
- Scannapieco E., Madau P., Woosley S., Heger A., Ferrara A., 2005, *ApJ*, 633, 1031
- Schaerer D., 2002, *A&A*, 382, 28
- Shara M. M., Ilkiewicz K., Mikolajewska J., Pagnotta A., Bode M. F., Crause L. A., Drozd K., Faherty J. K., Fuentes-Morales I., Grindlay J. E., Moffat A. F. J., Schmidtobreick L., Stephenson F. R., Tappert C., Zurek D., 2017, arXiv:1704.00086
- Shara M. M., Mizusawa T., Wehinger P., Zurek D., Martin C. D., Neill J. D., Forster K., Seibert M., 2012, *ApJ*, 758, 121
- Smidt J., Whalen D. J., Chatzopoulos E., Wiggins B., Chen K.-J., Kozyreva A., Even W., 2015, *ApJ*, 805, 44
- Smith A., Bromm V., Loeb A., 2017, *MNRAS*, 464, 2963
- Smith A., Safrank-Shrader C., Bromm V., Milosavljević M., 2015, *MNRAS*, 449, 4336
- Somers M. W., Ringwald F. A., Naylor T., 1997, *MNRAS*, 284, 359
- Spera M., Mapelli M., 2017, *MNRAS*, 470, 4739
- Stacy A., Bromm V., Lee A. T., 2016, *MNRAS*, 462, 1307
- Stacy A., Greif T. H., Bromm V., 2010, *MNRAS*, 403, 45
- Susa H., Hasegawa K., Tominaga N., 2014, *ApJ*, 792, 32
- Tanaka M., Moriya T. J., Yoshida N., 2013, *MNRAS*, 435, 2483
- Tolstov A., Nomoto K., Blinnikov S., Sorokina E., Quimby R., Baklanov P., 2017, *ApJ*, 835, 266
- Tominaga N., 2009, *ApJ*, 690, 526
- Umeda H., Nomoto K., 2003, *Nature*, 422, 871
- Volonteri M., Reines A., Atek H., Stark D. P., Trebitsch M., 2017, arXiv:1704.00753
- Wang F. Y., Bromm V., Greif T. H., Stacy A., Dai Z. G., Loeb A., Cheng K. S., 2012, *ApJ*, 760, 27
- Wang L., et al., 2017, arXiv:1710.07005
- Weinmann S. M., Lilly S. J., 2005, *ApJ*, 624, 526
- Whalen D. J., Even W., Frey L. H., Smidt J., Johnson J. L., Lovekin C. C., Fryer C. L., Stiavelli M., Holz D. E., Heger A., Woosley S. E., Hungerford A. L., 2013, *ApJ*, 777, 110
- Whalen D. J., Fryer C. L., Holz D. E., Heger A., Woosley S. E., Stiavelli M., Even W., Frey L. H., 2013, *ApJ*, 762, L6
- Wise J. H., Abel T., 2005, *ApJ*, 629, 615
- Woosley S. E., 2017, *ApJ*, 836, 244
- Woosley S. E., Blinnikov S., Heger A., 2007, *Nature*, 450, 390
- Yoon S.-C., Dierks A., Langer N., 2012, *A&A*, 542, A113
- Yoshida N., Abel T., Hernquist L., Sugiyama N., 2003, *ApJ*, 592, 645
- Yoshida T., Okita S., Umeda H., 2014, *MNRAS*, 438, 3119
- Young D. R., Smartt S. J., Mattila S., Tanvir N. R., Bersier D., Chambers K. C., Kaiser N., Tonry J. L., 2008, *A&A*, 489, 359
- Yusof N., Hirschi R., Meynet G., Crowther P. A., Ekström S., Frischknecht U., Georgy C., Abu Kassim H., Schnurr O., 2013, *MNRAS*, 433, 1114
- Zackrisson E., Binggeli C., Finlator K., Gnedin N. Y., Paardekooper J.-P., Shimizu I., Inoue A. K., Jensen H., Micheva G., Khochfar S., Dalla Vecchia C., 2017, *ApJ*, 836, 78
- Zackrisson E., Rydberg C.-E., Schaerer D., Östlin G., Tuli M., 2011, *ApJ*, 740, 13

This paper has been typeset from a $\text{T}_{\text{E}}\text{X}/\text{L}^{\text{A}}\text{T}_{\text{E}}\text{X}$ file prepared by the author.